Journal of Materials Chemistry A

ROYAL SOCIETY OF CHEMISTRY

PAPER

View Article Online
View Journal | View Issue

Cite this: *J. Mater. Chem. A*, 2025, **13**, 37970

Surface aluminization for enhancing oxidation resistance of the $Nb_{0.86}Hf_{0.14}FeSb$ thermoelectric element

Qihao Shen, [ab] Jinyu Gu,[a] Lei Wang,[a] Chao Wang,[a] Qingfeng Song,*[a] Xugui Xia,[a] Jincheng Liao,[a] Lidong Chen [ab] and Shengqiang Bai *[ab]

Received 25th July 2025
Accepted 2nd October 2025

DOI: 10.1039/d5ta06020f

rsc.li/materials-a

NbFeSb-based half-Heuslers (HHs) exhibit exceptional high-temperature thermoelectric (TE) performance, but their practical deployment is hindered by insufficient oxidation resistance. Here, a surface aluminization technology is introduced to improve oxidation resistance by forming *in situ* intermetallic compounds on the material surface. During this process, a dense coating with a thickness of 20–60 μm is formed through a solid/gas reaction between Al and the main constituents of HHs, exhibiting a lamellar structure composed of $Al_{13}Fe_4$, Al_3(Nb,Hf) and AlSb in sequence. The coating and substrate exhibit a robust metallurgical bond. Benefiting from the intrinsic oxidation resistance of aluminides, the coating serves as an effective diffusion barrier against oxygen penetration. Diffusion kinetics analysis reveals that the coating/substrate interface maintains an ultra-low diffusion rate in air, extending the predicted service life to over 10 years. The coated elements demonstrate negligible degradation in TE properties during prolonged aging at 973 K. The surface aluminization method effectively improves the feasibility and thermal stability of NbFeSb-based HHs in air, thus advancing their practical applications.

1. Introduction

Waste heat recovery has become a key issue in improving energy efficiency in the face of the growing energy crisis in contemporary society.[1–3] The environmentally friendly TE power generators, which can directly convert heat into electricity, have great potential, especially in low-grade waste heat recovery.[4–9]

As the determinant of theoretical conversion efficiency of TE devices, the dimensionless figure of merit (zT) of TE materials became the research focus in the past few decades, and many novel TE materials have been discovered.[10–20] Among them, HH compounds are considered as the ideal candidates for high-temperature power generators due to their excellent TE and mechanical properties.[14,15,21–26] With a deeper understanding of thermal and electrical transport mechanisms, the TE performance of HHs has been greatly improved. Recently, the zT of p-type NbFeSb and n-type ZrNiSn based HHs reached 1.60 and 1.12,[14,15] respectively. The energy conversion efficiency of single and segmented HH devices has crossed 11.1% and 13.3%, respectively.[27]

In practical services, the thermal stability of TE materials and devices is more critical than their zT and efficiency.[28–30] Most TE materials,[31–38] including Mg_2Si, $CoSb_3$, HH, *etc.*, exhibit poor oxidation resistance, especially at high temperatures and in an air environment. The formation of electrically insulating oxides results in the change of chemical composition, thereby causing deterioration of zT.[39] For example, in $CoSb_3$-based skutterudite, the formation of Sb_2O_3 significantly degrades electrical conductivity, which causes a 29.2% deterioration in zT.[32] Easily oxidized p-type (Zr,Hf,Ti)Co(Sb,Sn) exhibits a 49.5% decrease of output power in a TE generator after working in air for 115 hours at a temperature gradient of 823 K/294 K.[35] Similarly, the output power of an n-type (Zr,Hf)Ni(Sb,Sn) TE device drops to 61% of the initial value after operation at 778 K/300 K for 15 days in air.[34]

To make the applications of HHs feasible in air, the oxidation resistance should be considered as an essential evaluation criterion. The strong composition–property coupling inherent in TE materials presents a critical challenge in developing oxidation-resistant materials. Some efforts have been made to develop protective coatings for TE materials. For example, 8 mol% yttria-stabilized zirconia (YSZ), yttria (Y_2O_3) and alumina (Al_2O_3) coatings are designed for Mg_2Si.[40] Nevertheless, conventional plasma spraying techniques struggle to prevent process-induced thermal damage of TE materials. Aerogel coatings have been used to protect $CoSb_3$-based skutterudites. However, the interconnected micro and mesopores in aerogels provide oxygen migration channels, which cause progressive degradation during long-term operation.[39] The designed CrSi coating for (Zr,Ti)Ni(Sn,Sb) and (Zr,Ti)Co(Sn,Sb) prepared by

[a]*State Key Laboratory of High Performance Ceramics and Superfine Microstructure, Shanghai Institute of Ceramics, Chinese Academy of Sciences, Shanghai 200050, China. E-mail: qfsong@mail.sic.ac.cn; bsq@mail.sic.ac.cn*

[b]*Center of Materials Science and Optoelectronics Engineering, University of Chinese Academy of Sciences, Beijing 100049, China*

magnetron sputtering can prevent the diffusion of oxygen, but the limits of coating thickness (<2 μm) severely affect its service life.[41] By controlled oxidation treatments, *in situ* dense oxide layers can be formed on the surface of n-type (Zr,Hf)Ni(SnSb) and p-type (Zr,Hf)Co(Sb,Sn).[34,36] However, the formation of such dense oxide coatings is governed by chemical composition, thereby restricting the applicability of this strategy to specific material systems.

As high-temperature TE materials, $Nb_{0.86}Hf_{0.14}FeSb$-based half-Heusler (NHFS) alloys inevitably undergo oxidative degradation during service in oxygen-containing environments. Conventional spray or deposition coatings often suffer from interfacial compatibility issues. The pack cementation method, as an in situ diffusion coating technique, utilizes intrinsic elements from NHFS to form a lamellar aluminide coating on the surface. Benefiting from interlayer interdiffusion and matched coefficients of thermal expansion, a robust metallurgical bond forms at the coating/substrate interface. This aluminide coating effectively blocks inward oxygen diffusion, preventing oxidation-induced cracking. Although interfacial diffusion occurs at elevated temperatures, the thickening rate of the diffusion layer is significantly suppressed due to attenuation of the aluminum concentration gradient. Furthermore, coated NHFS elements exhibit negligible degradation in TE performance after aging at 973 K, demonstrating exceptional service stability of surface-aluminized NHFS in air.

2. Materials and methods

2.1. Synthesis of NHFS

$Nb_{0.86}Hf_{0.14}FeSb$ was synthesized by induction melting in a vacuum. High-purity raw materials of Nb (99.9%, Alfa Aesar), Hf (99.9%, Alfa Aesar), Fe (99.99%, Alfa Aesar), Sb (99.95%, Alfa Aesar) were weighed in stoichiometric mass and melted by the induction melting method. The obtained ingots were then crushed and ball-milled into fine powders, followed by consolidation using hot-pressure sintering under 60 MPa pressure at 1243 K and holding for 15 min. The details of the synthesis process are shown in our previous studies.[42] The sintered wafer was cut into small pieces for coating experiments and aging tests in air.

2.2. Pack cementation aluminizing

The NHFS samples were aluminized by the pack cementation method. The composition of the coating powder mixture was 30 wt% Al, 4 wt% $AlCl_3$, 66 wt% Al_2O_3. The powders were mixed well by high-energy ball milling. The NHFS samples covered with coating powders were placed in an alumina crucible, then placed in a quartz tube and encapsulated under vacuum. The encapsulated quartz tube was placed in a muffle furnace and held at 973–1073 K.

2.3. Aging test

The uncoated NHFS and coated NHFS samples were placed in open quartz crucibles and placed in a muffle furnace in air, and aged at 873 K, 923 K and 973 K. The mass of the samples before and after aging was weighed using an electronic balance (QUINTIX35–1CN) with an accuracy of 10^{-5} g.

2.4. Characterization

X-ray diffraction analysis (XRD, Bruker, Cu Kα) and micro-region XRD (micro-XRD, Rigaku Rint2000, Cu Kα) were performed to determine the phase composition. Scanning electron microscopy (SEM, ZEISS Supra 55) coupled with energy-dispersive spectroscopy (EDS, OXFORD Aztec X-Max80) was used to investigate the microstructure and morphology. The thickness of the diffusion layer was measured from the SEM image. The Seebeck coefficient (S) and electrical conductivity (σ) were simultaneously measured from room temperature to 1000 K by the ordinary four-probe DC method using ZEM-3 (Ulvac-Riko) in a sealed chamber with a small amount of helium gas.

3. Results and discussion

3.1. Characterization of the aluminide coating

An aluminide coating was fabricated on NHFS *via* pack cementation, in which the NHFS samples were embedded in a mixture of Al, $AlCl_3$ and Al_2O_3 powders and heated at 973–1073 K. $AlCl_3$ was introduced as an activator to promote aluminizing kinetics. The schematic diagram of the coating formation mechanism is shown in Fig. 1(a). The preparation process consists of two steps: the generation of active aluminum and the diffusion growth of the coating layer. At high temperatures, $AlCl_3$ decomposes to generate gaseous $AlCl_2$ and AlCl,[43,44] which subsequently release active Al atoms ([Al]). [Al] adsorbs to the surface of the substrate and dissolves into NHFS to form a solid solution. When Al reaches a certain concentration, the aluminized layer starts to form. When the processing temperature is below 973 K, the NHFS surface cannot form a continuous aluminide coating due to insufficient reaction kinetics. Conversely, at temperatures exceeding 1073 K, the quartz tube reacts with $AlCl_3$, introducing silicon impurities into the aluminide layer. Therefore, the optimum processing temperature for coating fabrication is 973–1073 K.

The surface secondary electron image of coated NHFS is presented in SI Fig. A1. The rough surface is a characteristic metallurgical phenomenon inherent to pack cementation processes, which originates from non-uniform [Al] concentration gradients. The cross-sectional micro-XRD and surface XRD patterns of the aluminide layer are shown in Fig. 1(b) to determine the phase composition. The diffraction peaks of three aluminide phases in the coating are observed in surface XRD, namely, Al_3(Nb,Hf), AlSb, and $Al_{13}Fe_4$. The absence of the NHFS peak indicates that the coating is thick enough beyond the detection depth of surficial XRD. The phase composition of the coating is also supported by cross-sectional micro-XRD. Due to the relatively large detection range of micro-XRD, the host phase NHFS is detected. This demonstrates compositional homogeneity throughout the coating. The overall reaction at the coating interface is:

$$Al + (Nb,Hf)FeSb \rightarrow Al_3(Nb,Hf) + AlSb + Al_{13}Fe_4$$

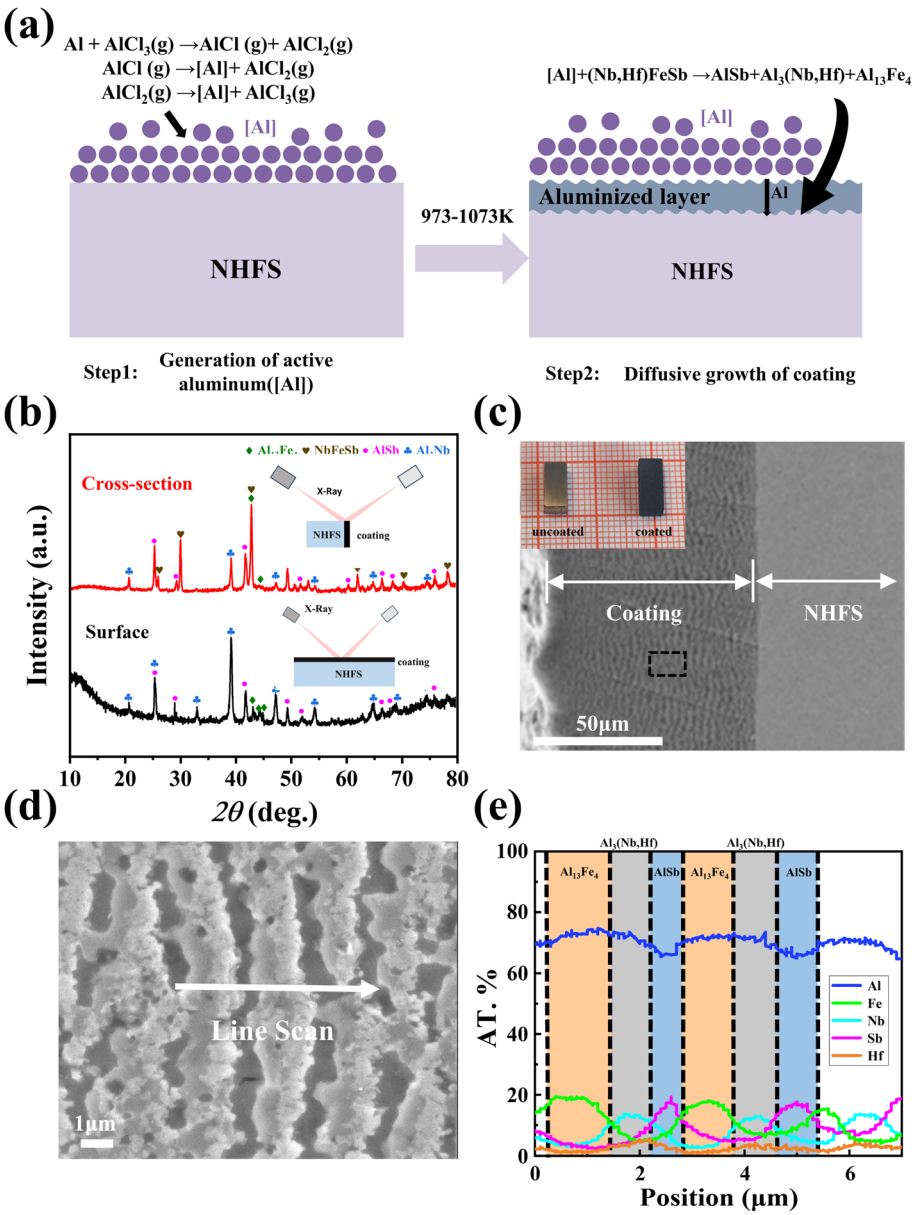

Fig. 1 (a) Schematic diagram of the coating formation mechanism; (b) cross-sectional micro-XRD and surface XRD patterns of the aluminide layer; (c and d) cross-sectional SEM images of the coated NHFS: (c) overall view and (d) the amplified view of the selected black dashed rectangle area in (c); (e) the corresponding elemental line-scan profiling along the white arrow in (d).

The cross-sectional secondary electron image of the coated NHFS is shown in Fig. 1(c). The coating exhibits no cracks or pores and maintains strong interfacial bonding with the substrate. The secondary electron image and elemental line profiling of the amplified view of the selected area in Fig. 1(c) are shown in Fig. 1(d) and (e). Combined with elemental mapping results (SI Fig. A2), Al is uniformly distributed throughout the coating, while Nb, Fe, and Sb are distributed as a hierarchical structure. The Al content is maintained at approximately 72%. The observed decline in Al content is attributable to the lower Al concentration in AlSb than that in both $Al_3(Nb,Hf)$ and $Al_{13}Fe_4$. The observed layered architecture demonstrates sequential formation of three aluminide phases within localized regions. The reaction enthalpy (ΔH) values of the compounds directly correlate with their formation tendency, where lower ΔH indicates higher thermodynamic stability. As shown in SI Fig. A3, the progressively decreasing ΔH values of Al_3Nb, AlSb and $Al_{13}Fe_4$ (−0.66, −0.51, and −0.43 eV/Al) align with their distribution in the layered structure. These findings align with the formation mechanism of alternate layered oxides.[36] Thus, the distinct reaction enthalpies drive sequential precipitation of these phases in constrained diffusion zones.

Due to the interdiffusion of Al, a robust metallurgical bond forms at the coating/substrate interface, possessing

a coefficient of thermal expansion (CTE) closely aligned with that of NHFS (Al_3Nb ~9.6 × 10^{-6} K^{-1}, $Al_{13}Fe_4$ ~ 11.9 × 10^{-6} K^{-1}, and NHFS ~10 × 10^{-6} K^{-1}),[45,46] effectively mitigating CTE mismatch between the coating and substrate. In addition, each aluminide layer maintains a thickness of merely 1–2 μm, effectively suppressing thermal stress within the coating. The interlayer diffusion significantly enhances the bonding strength, thereby preventing any observable cracking at elevated temperatures. In addition, the thickness of the coating can be precisely controlled to meet specific application requirements. The thickness shows a parabolic growth with holding time (see SI Fig. A4), indicating that the coating process is dominated by the diffusion process of Al.[44] When the thickness is too thin, the substrate may become exposed, leading to insufficient protective performance. Conversely, an excessively thick coating can result in cracking at the edges and corners (see SI Fig. A5). Considering the protective effect, the optimal thickness of the coating is in the range of 20–60 μm.

3.2. Antioxidant properties and kinetic analysis

To ascertain the oxidation resistance of the coating, long-term oxidation aging tests were conducted in air at 873 K, 923 K and 973 K. The mass gain of uncoated and coated NHFS over time is presented in Fig. 2(a) and (b). For uncoated NHFS, the mass gain shows a sudden transition to exponential growth kinetics after an initial stabilization phase. The average oxidation rates are 0.46, 3.28 and 7.28 mg per cm^2 per hour at 873 K, 923 K, and 973 K, respectively. Compared to uncoated samples, the mass gain rates of the coated NHFS drop by ~99%. The parabolic rate constants (K_p) for coated NHFS are 3.82 × 10^{-7}, 3.94 × 10^{-7} and 5.68 × 10^{-7} mg^2 cm^{-4} s^{-1} at 873 K, 923 K and 973 K, respectively (SI Fig. A6). The introduction of the coating transforms the weight gain curve from linear to parabolic, indicating a shift from reaction-controlled to a diffusion-controlled process.

Fig. 2(c) shows the appearance of uncoated and coated NHFS after aging at 973 K. The uncoated sample exhibits severe cracking and oxidation after 10 h, resulting in complete material failure. The cracks first appeared at the corners, which are the stress concentration zones. Under prolonged aging exposure, the progressive inward propagation of cracks ultimately induces the complete failure of NHFS. The catastrophic oxidation renders NHFS completely unsuitable for any application in oxygen-containing atmospheres. With the coating applied, the sample exhibits no visible degradation after aging at 973 K for 720 h. This remarkable improvement originates from the

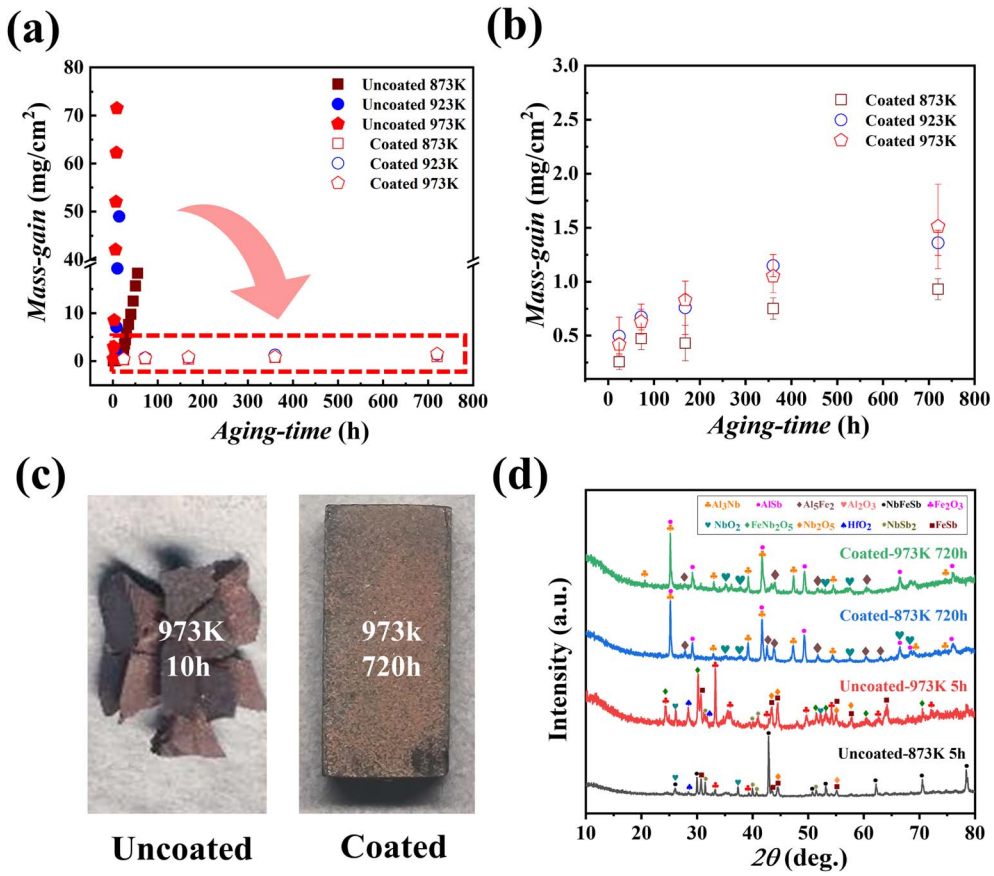

Fig. 2 (a) Mass-gain *vs.* aging time for uncoated and coated NHFS at different aging temperatures; (b) detailed data of the coated samples in (a); (c) the appearance of uncoated and coated NHFS after aging at 973 K for 10 h and 720 h, respectively. (d) The XRD patterns of uncoated and coated NHFS after aging at different temperatures.

formation of thermally stable Al_2O_3, as confirmed by XRD analysis and EDS results (Fig. 2(d) and SI Fig. A7).

The XRD patterns of uncoated and coated NHFS after aging at 873 K and 973 K are shown in Fig. 2(d). For coated NHFS, four phases—Al_2O_3, Al_3Nb, AlSb and Al_5Fe_2—are observed. Compared to the sample before aging, $Al_{13}Fe_4$ transforms into Al_5Fe_2, while Al_3Nb and AlSb phases remain within the coating matrix. SI Table A1 shows the calculated enthalpies of formation of the possible reaction for the oxidation process of the aluminide coating. All three aluminum compounds can generate Al_2O_3 and corresponding oxides upon reaction with O_2. This endows the coating with both oxidation resistance and self-healing capability. Fig. 2(d) also presents the XRD patterns of the uncoated NHFS after aging for 5 hours at 873 K and 973 K. The diffraction peaks of eight phases are observed, namely NbFeSb, Fe_2O_3, Nb_2O_5, NbO_2, HfO_2, $FeNb_2O_6$, FeSb and $NbSb_2$. The CTEs for the main oxidation products are shown in SI Table A2. Due to the large difference in CTE between NHFS (9.0×10^{-6} K^{-1}) and Fe_2O_3 ($\sim 12.0 \times 10^{-6}$ K^{-1}), Nb_2O_5 ($\sim 5.9 \times 10^{-6}$ K^{-1}), HfO_2 ($\sim 5.8 \times 10^{-6}$ K^{-1}),[47–49] and the relatively high Pilling-Bedworth ratio of Nb/Nb_2O_5 (2.67) and Fe/Fe_2O_3 (2.09),[50] substantial intrinsic compressive stresses are generated within the oxides and then evolved into cracks.

The cross-sectional BSE image of the uncoated NHFS after aging at 873 K for 20 h and the corresponding elemental line-scan profiles along the white arrows are shown in Fig. 3(a)

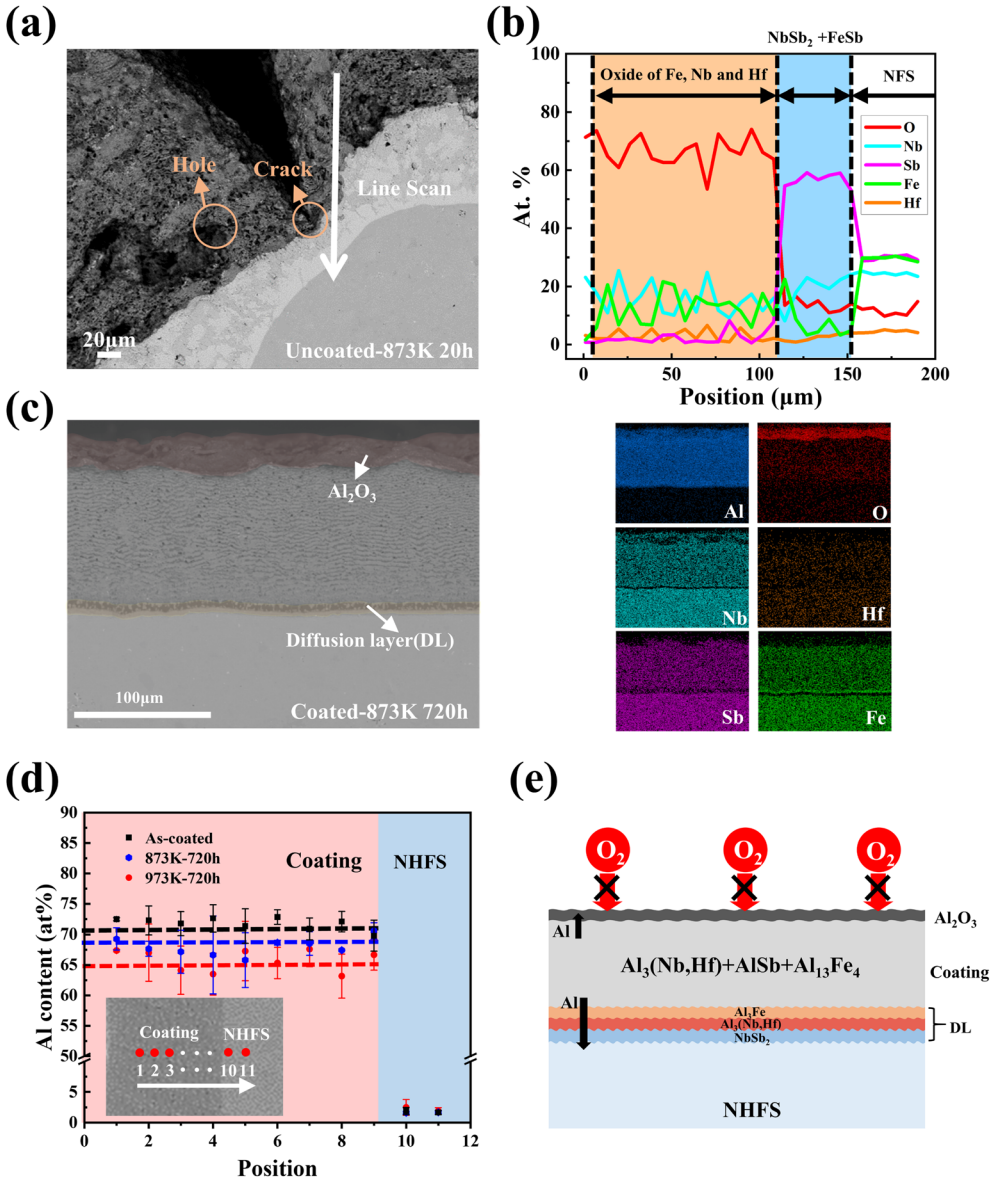

Fig. 3 (a) The cross-sectional BSE image of the uncoated NHFS after aging at 873 K for 20 h; (b) the elemental line-scan profiles along the white arrow marked in (a); (c) the cross-sectional BSE image of the coated NHFS after aging at 873 K for 720 h in air and corresponding elemental mapping results; (d) Al content distribution in the coating layer for coated NHFS; (e) schematic diagram of the oxidation protection mechanism by the aluminized coating layer on the surface of the NHFS sample.

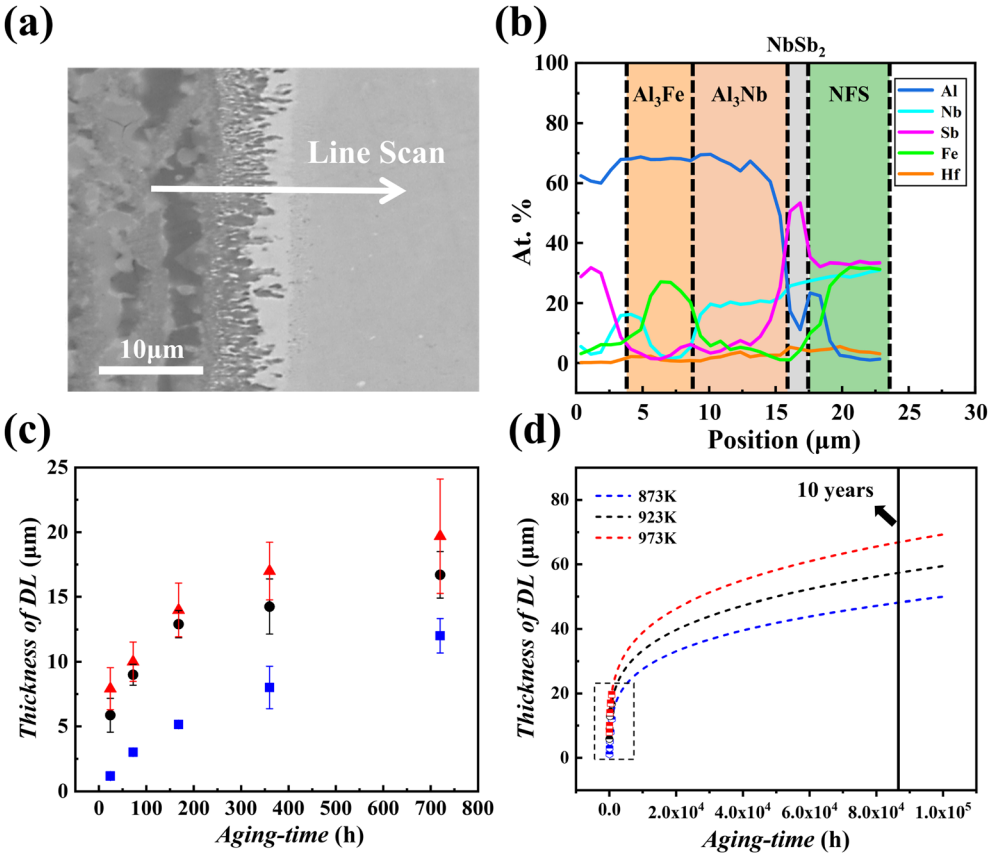

Fig. 4 (a) The BSE images of the diffusion layer of the coated NHFS sample after aging at 973 K for 720 h; (b) the elemental line-scan profiles along the white arrows marked in (a). (c) The thickness of DL *vs.* aging time; (d) predicted variation of DL thickness *vs.* aging time at different temperatures.

and (b). From the BSE image observation, a two-layer structure is formed on the surface of the material. The elemental line-scan results indicate that the outer layer is composed of Fe, Nb and Hf oxides. The oxide layer exhibits a porous structure with visible cracks. The inner layer is composed of FeSb and $NbSb_2$ mixtures. Unfortunately, these oxide layer structures fail to inhibit further oxidation. The total thickness of these two oxidation layers has been over 200 μm, which was caused by the accelerated oxidation rate in the porous structures.

Fig. 3(c) shows a representative backscattered electron (BSE) image and corresponding elemental mapping result of the coated NHFS after aging at 873 K for 720 h in air, revealing characteristic structure evolution. Compared to uncoated NHFS, the coated NHFS maintains structural integrity throughout the aging process. The Al_2O_3 surface layer serves as an effective barrier against inward diffusion of O_2. Notably, a significant diffusion occurs at the interface. Al gradually diffuses into NHFS, forming a ~15 μm diffusion layer (DL). This further strengthens the bonding between the aluminide coating and NHFS. Al content distribution in the coating layer of coated NHFS, from the coating to the substrate, before and after long-term aging at 873 K and 973 K is shown in Fig. 3(d). After aging at 873 K and 973 K for 720 h, the Al content decreases by 3.83% and 6.02% compared to the coated NHFS before aging, respectively. This is primarily attributed to diffusion into the substrate and the self-healing of the protective layer.

The BSE image of the diffusion layer and the corresponding elemental line-scan profiles along the white arrows are shown in Fig. 4(a) and (b). It indicates that the diffusion layer consists of Al_3Fe, Al_3Nb and $NbSb_2$. The thickness of the diffusion layer increases progressively with both elevated aging temperature and prolonged exposure time. This may adversely affect the performance of NHFS.

The cross-sectional morphology of the coated NHFS exhibits negligible microstructural degradation following prolonged aging at temperatures below 973 K. The reaction-diffusion kinetics model is introduced to describe the kinetics of the diffusion layer (see SI Note A1).[51] The thickness of DL at different aging temperatures is determined from the cross-sectional SEM images (see SI Fig. A9) and shown in Fig. 4(c). The thickness of the diffusion layer follows a parabolic relationship with time. This is attributed to the depletion of additional aluminum sources and the decline in the aluminum concentration gradient, which significantly suppresses the growth rate of the diffusion layer.

The parameters, including the chemical reaction constant k_0, diffusion constant k_1, activation energy of chemical reaction E_0, and activation energy of diffusion E_1, are calculated from the

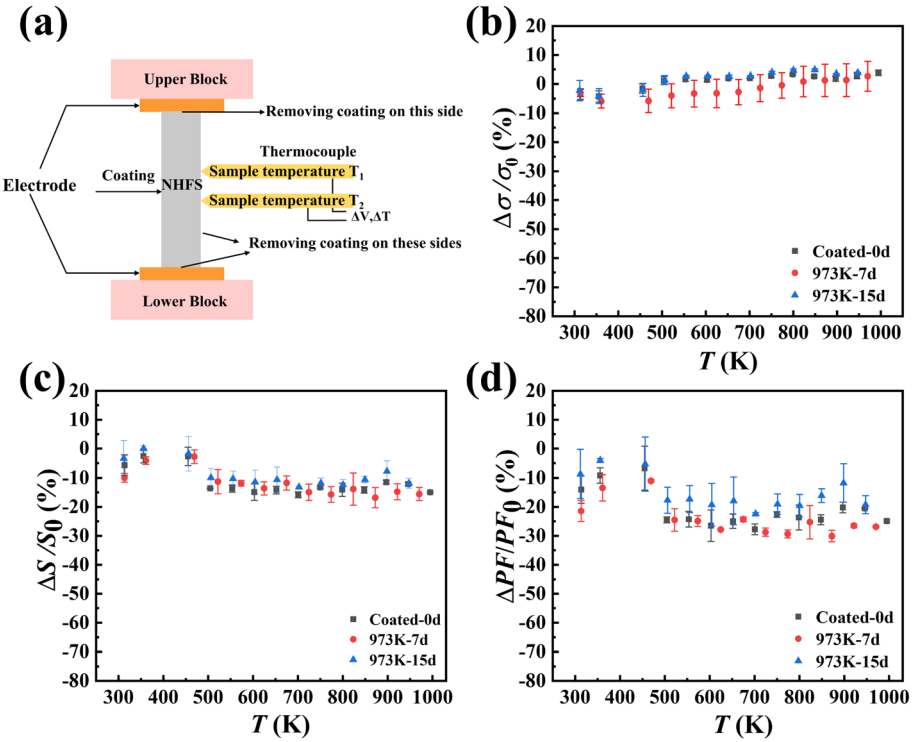

Fig. 5 (a) Schematic diagram of the electrical performance test. (b–d) The relative change in electric properties for coated NHFS before and after aging at 973 K for 7 d and 15 d, where σ_0, S_0 and PF_0 represent the electrical conductivity, Seebeck coefficient and power factor of as-prepared coated NHFS.

time-dependent thickness of the diffusion layer from 873 K to 973 K and are shown in SI Table A3. The obtained E_0 and E_1 are 230.00 kJ mol^{-1} and 91.09 kJ mol^{-1}, respectively, suggesting that the formation of DL is a process controlled by diffusion. Based on the kinetic data, the relationship between the predicted thickness of DL and time is shown in Fig. 4(d). After aging at 873 K, 923 K, and 973 K for 10 years, the predicted DL thicknesses are only 48.32 μm, 57.53 μm and 67.02 μm, respectively, which are within the acceptable range for the practical TE devices.

3.3. Electrical performance analysis

The electrical properties of samples with coatings were characterized to evaluate the change in thermoelectric device performance. Before the measurement, the coatings on the upper, lower, and one side surfaces were removed to achieve good contacts with the electrodes and thermocouples (see Fig. 5(a)). The relative changes in electric properties for coated NHFS before and after aging at 973 K for 7 d and 15 d in air are summarized in Fig. 5(b–d), where σ_0, S_0 and PF_0 represent the electrical conductivity, Seebeck coefficient and power factor (PF $= S^2\sigma$) of as-prepared NHFS. The σ of Al_3Nb is higher than that of NHFS, but the σ of AlSb is much lower (see in SI Fig. A10). Based on the theory of thermoelectric composite materials (see SI Note A2), the average σ of AlSb and Al_3Nb are comparable to that of the NHFS substrate, resulting in an unchanged σ of the coated sample. Meanwhile, the S of AlSb and Al_3Nb is both lower than that of NHFS, which leads to the S degradation of the coated sample. After complete removal of the coating, the electrical properties return to those of the as-prepared state (see in SI Fig. A12). Compared to the coated NHFS before aging, the electrical performance exhibited no deterioration after aging in air at 973 K. This indicates that under the protective coating, the material's internal structure remained completely intact, allowing it to maintain optimal electrical performance.

4. Conclusion

To improve the oxidation resistance of NHFS, we prepared a dense layered coating by surface aluminizing using a pack cementation method, in which the NHFS samples are embedded in the mixture of Al, $AlCl_3$ and Al_2O_3 powders and then heated at 973∼1073 K. During this process, a dense coating with a thickness of 20–60 μm is formed by the solid/gas reactions between Al and the main constituents of NHFS, which are lamellar-structured and composed of $Al_{13}Fe_4$, Al_3(Nb,Hf) and AlSb. Such a lamellar-structured coating acts as an effective barrier for blocking oxygen diffusion and protects the HH substrate from oxidation. The mass-gain rate of coated NHFS decreases by 99% compared to the uncoated sample at 873–973 K for 30 days. Moreover, the *in situ* coating maintains structural integrity throughout prolonged aging tests, with neither observable crack propagation nor interfacial delamination. The coated NHFS exhibits no deterioration in TE properties after aging in air at 973 K, demonstrating excellent feasibility of NHFS-based TE devices operating in air.

Author contributions

Qihao Shen: writing – original draft, data curation, methodology, investigation, resources. Jinyu Gu: data curation. Lei Wang: investigation. Qingfeng Song: data curation, investigation, resources, funding acquisition. Chao Wang: assistant for element fabrication. Xugui Xia: assistant for element fabrication. Jincheng Liao: assistant for characterization. Lidong Chen: validation, writing – review & editing. Shengqiang Bai: methodology, writing – review & editing, supervision, validation, funding acquisition.

Conflicts of interest

The authors declare that they have no known competing financial interests or personal relationships that could have appeared to influence the work reported in this paper.

Data availability

Data will be made available on request. Supplementary information is available. See DOI: https://doi.org/10.1039/d5ta06020f.

Acknowledgements

This work was financially supported by the National Key Research and Development Program of China (Grant No. 2023YFB3809400) and the National Natural Science Foundation of China (NSFC) (Grant No. U2141208).

References

1 S. Hur, S. Kim, H. S. Kim, A. Kumar, C. Kwon, J. Shin, H. Kang, T. H. Sung, J. Ryu, J. M. Baik and H. C. Song, *Nano Energy*, 2023, **114**, 108596.
2 K. Imasato, S. D. Kang and G. J. Snyder, *Energy Environ. Sci.*, 2019, **12**, 965–971.
3 B. Zhao, K. Chen, S. Buddhiraju, G. Bhatt, M. Lipson and S. Fan, *Nano Energy*, 2017, **41**, 344–350.
4 N. V. Burnete, F. Mariasiu, C. Depcik, I. Barabas and D. Moldovanu, *Prog. Energy Combust. Sci.*, 2022, **91**, 101009.
5 H. Li, C. Chen, J. Cheng, Y. Xia, S. Lyu, K. Liu, W. Xue, D. Shen, W. Wang, Q. Zhang and Y. Chen, *Nano Energy*, 2025, **136**, 110690.
6 T. Xing, Q. Song, P. Qiu, Q. Zhang, M. Gu, X. Xia, J. Liao, X. Shi and L. Chen, *Energy Environ. Sci.*, 2021, **14**, 995–1003.
7 J. Cao, J. Dong, J. Wu and A. Suwardi, *ACS Nano*, 2025, **19**, 26249–26258.
8 G. Dong, J. Feng, G. Qiu, Y. Yang, Q. Chen, Y. Xiong, H. Wu, Y. Ling, L. Xi, C. Long, J. Lu, Y. Qiao, G. Li, J. Li, R. Liu and R. Sun, *Nat. Commun.*, 2024, **15**, 9695.
9 Z. Gong, A. Suwardi and J. Cao, *Adv. Funct. Mater.*, 2025, 2423371.
10 C. Wood, *Rep. Prog. Phys.*, 1988, **51**, 459.
11 Z. Bu, X. Zhang, B. Shan, J. Tang, H. Liu, Z. Chen, S. Lin, W. Li and Y. Pei, *Sci. Adv.*, 2021, **7**, eabf2738.
12 Z. Zhang, C. Ming, Q. Song, L. Wang, H. Chen, J. Liao, C. Wang, L. Chen and S. Bai, *Acta Mater.*, 2025, **287**, 120806.
13 X. Zhang, Z. Bu, S. Lin, Z. Chen, W. Li and Y. Pei, *Joule*, 2020, **4**, 986–1003.
14 J. Yu, C. Fu, Y. Liu, K. Xia, U. Aydemir, T. C. Chasapis, G. J. Snyder, X. Zhao and T. Zhu, *Adv. Energy Mater.*, 2018, **8**, 1701313.
15 X. Yang, Y. Liu, R. Min, X. Jiang, Y. Liu, Y. Zhang and H. Chen, *Acta Mater.*, 2025, **284**, 120626.
16 B. C. Sales, D. Mandrus and R. K. Williams, *Science*, 1996, **272**, 1325–1328.
17 B. Poudel, Q. Hao, Y. Ma, Y. Lan, A. Minnich, B. Yu, X. Yan, D. Wang, A. Muto, D. Vashaee, X. Chen, J. Liu, M. S. Dresselhaus, G. Chen and Z. Ren, *Science*, 2008, **320**, 634–638.
18 Z. Liu, J. Zhu, X. Tong, S. Niu and W. Zhao, *J. Adv. Ceram.*, 2020, **9**, 647–673.
19 L. Fu, M. Yin, D. Wu, W. Li, D. Feng, L. Huang and J. He, *Energy Environ. Sci.*, 2017, **10**, 2030–2040.
20 T. Cao, X. Shi, M. Li, B. Hu, W. Chen, W. Liu, W. Lyu, J. MacLeod and Z. Chen, *eScience*, 2023, **3**, 100122.
21 T. Zhu, C. Fu, H. Xie, Y. Liu and X. Zhao, *Adv. Energy Mater.*, 2015, **5**, 1500588.
22 H. Zhu, R. He, J. Mao, Q. Zhu, C. Li, J. Sun, W. Ren, Y. Wang, Z. Liu, Z. Tang, A. Sotnikov, Z. Wang, D. Broido, D. J. Singh, G. Chen, K. Nielsch and Z. Ren, *Nat. Commun.*, 2018, **9**, 2497.
23 H. Zhao, B. Cao, S. Li, N. Liu, J. Shen, S. Li, J. Jian, L. Gu, Y. Pei, G. J. Snyder, Z. Ren and X. Chen, *Adv. Energy Mater.*, 2017, **7**, 1700446.
24 K. S. Kim, Y.-M. Kim, H. Mun, J. Kim, J. Park, A. Y. Borisevich, K. H. Lee and S. W. Kim, *Adv. Mater.*, 2017, **29**, 1702091.
25 G. Joshi, X. Yan, H. Wang, W. Liu, G. Chen and Z. Ren, *Adv. Energy Mater.*, 2011, **1**, 643–647.
26 G. Rogl, A. Grytsiv, M. Gürth, A. Tavassoli, C. Ebner, A. Wünschek, S. Puchegger, V. Soprunyuk, W. Schranz, E. Bauer, H. Müller, M. Zehetbauer and P. Rogl, *Acta Mater.*, 2016, **107**, 178–195.
27 R. Liu, Y. Xing, J. Liao, X. Xia, C. Wang, C. Zhu, F. Xu, Z. Chen, L. Chen, J. Huang and S. Bai, *Nat. Commun.*, 2022, **13**, 7738.
28 L. Zhang, X. Chen, Y. Tang, L. Shi, G. J. Snyder, J. B. Goodenough and J. Zhou, *J. Mater. Chem. A*, 2016, **4**, 17726–17731.
29 P. Qiu, J. Cheng, J. Chai, X. Du, X. Xia, C. Ming, C. Zhu, J. Yang, Y.-Y. Sun, F. Xu, X. Shi and L. Chen, *Adv. Energy Mater.*, 2022, **12**, 2200247.
30 W. Wu, G. Ren, X. Chen, Y. Liu, Z. Zhou, J. Song, Y. Shi, J. Jiang and Y. Lin, *J. Mater. Chem. A*, 2021, **9**, 3209–3230.
31 F. D'Isanto, F. Smeacetto, M. J. Reece, K. Chen and M. Salvo, *Ceram. Int.*, 2020, **46**, 24312–24317.
32 D. Zhao, C. Tian, S. Tang, Y. Liu and L. Chen, *J. Alloys Compd.*, 2010, **504**, 552–558.
33 P. Qiu, X. Xia, X. Huang, M. Gu, Y. Qiu and L. Chen, *J. Alloys Compd.*, 2014, **612**, 365–371.
34 L. Wang, Q. Song, J. Gu, C. Wang, S. Bai and L. Chen, *Corros. Sci.*, 2023, **225**, 111606.

35 H. B. Kang, U. Saparamadu, A. Nozariasbmarz, W. Li, H. Zhu, B. Poudel and S. Priya, *ACS Appl. Mater. Interfaces*, 2020, **12**, 36706–36714.
36 J. Gu, L. Wang, Q. Song, C. Wang, X. Xia, J. Liao, Y. Sun, L. Chen and S. Bai, *J. Mater. Sci. Technol.*, 2023, **148**, 242–249.
37 O. Appel, S. Cohen, O. Beeri, N. Shamir, Y. Gelbstein and S. Zalkind, *Materials*, 2018, **11**, 2296.
38 O. Appel, G. Breuer, S. Cohen, O. Beeri, T. Kyratsi, Y. Gelbstein and S. Zalkind, *Materials*, 2019, **12**, 1509.
39 Q. Zhang, X. Huang, S. Bai, X. Shi, C. Uher and L. Chen, *Adv. Eng. Mater.*, 2016, **18**, 194–213.
40 S. H. Park, Y. Kim and C. Y. Yoo, *Ceram. Int.*, 2016, **42**, 10279–10288.
41 M. Gurtaran, Z. Zhang, X. Li and H. Dong, *J. Mater. Res. Technol.*, 2024, **32**, 3288–3301.
42 Y. Xing, R. Liu, J. Liao, C. Wang, Q. Zhang, Q. Song, X. Xia, T. Zhu, S. Bai and L. Chen, *Joule*, 2020, **4**, 2475–2483.
43 Y. Sun, J. Dong, P. Zhao and B. Dou, *Surf. Coat. Technol.*, 2017, **330**, 234–240.
44 S. Rashidi, J. P. Choi, J. W. Stevenson, A. Pandey and R. K. Gupta, *Corros. Sci.*, 2020, **174**, 108835.
45 S. Saha, T. Z. Todorova and J. W. Zwanziger, *Acta Mater.*, 2015, **89**, 109–115.
46 S. Teslia, M. Teslia, Q. Sun and A. Stepanchuk, *Vacuum*, 2023, **218**, 112590.
47 M. Takeda, T. Onishi, S. Nakakubo and S. Fujimoto, *Mater. Trans.*, 2009, **50**, 2242–2246.
48 W. R. Manning, O. Hunter Jr, F. W. Calderwood and D. W. Stacy, *J. Am. Ceram. Soc.*, 1972, **55**, 342–347.
49 R. N. Patil and E. C. Subbarao, *J. Appl. Crystallogr.*, 1969, **2**, 281–288.
50 C. Proff, S. Abolhassani and C. Lemaignan, *J. Nucl. Mater.*, 2013, **432**, 222–238.
51 J. Chu, J. Huang, R. Liu, J. Liao, X. Xia, Q. Zhang, C. Wang, M. Gu, S. Bai, X. Shi and L. Chen, *Nat. Commun.*, 2020, **11**, 2723.